
Investigation of open channel flow with unsubmerged rigid vegetation by the lattice Boltzmann method*

He-fang JING^{1,2†}, Yin-juan CAI², Wei-hong WANG²,
Ya-kun GUO^{3‡}, Chun-guang LI^{2§} and Yu-chuan BAI¹

1. State Key Laboratory of Hydraulic Engineering Simulation and Safety, Tianjin University, Tianjin 300350, China;

2. Research Institute of Numerical Computation and Engineering Applications, North Minzu University, Yinchuan 750021, China.

3. Faculty of Engineering & Informatics, University of Bradford, Bradford, BD7 1DP, UK.

Abstract: Aquatic vegetation can significantly affect flow structure, sediment transport, bed scour and water quality in rivers, lakes, reservoirs and open channels. In this study, the lattice Boltzmann method is applied for performing the two dimensional numerical simulation of the flow structure in a flume with rigid vegetation. A multi-relaxation time model is applied to improve the stability of the numerical scheme for flow with high Reynolds number. The vegetation induced drag force is added in lattice Boltzmann equation model with the algorithm of multi-relaxation time in order to improve the simulation accuracy,. Numerical simulations are performed for a wide range of flow and vegetation conditions and are validated by comparing with the laboratory experiments. Analysis of the simulated and experimentally measured flow field shows that the numerical simulation can satisfactorily reproduce the laboratory experiments, indicating that the proposed lattice Boltzmann model has high accuracy for simulating flow-vegetation interaction in open channel.

Key Words: Lattice Boltzmann method; multi-relaxation time model; aquatic vegetation; drag force; open channel flow

1. Introduction

Aquatic vegetation is one of the important components in water flow system in natural rivers,

* Project supported by the Funds for National Natural Science Foundation of China (grant number: 11861003 and 11761005).

† **Biography:** He-fang JING (1970--), male, Ph.D., Professor. **Email:** jinghef@163.com. **Tel:** +86 951 2068010 (O), +86 13259510918(M) **Address:** Research Institute of Numerical Computation and Engineering Applications, North Minzu University, Yinchuan 750021, China.

‡ Corresponding author, Email: y.guo16@bradford.ac.uk

§ Correspond author, Email: cglizd@hotmail.com

28 lakes, reservoirs and open channels. Aquatic vegetation can significantly affect not only the
29 flow structure, but also the sediment transport, bed deformation, navigation, stability of banks
30 and flood control equipment ^[1,2]. Due to the practical environmental and engineering
31 importance, extensive studies have been carried out to investigate the flow-vegetation
32 interaction and its effect on flow system by using the laboratory experiments, numerical
33 simulation and occasionally the field observations ^[3-7]. In general, comparing with the
34 numerical simulation and laboratory experiments, it is more difficult to conduct field
35 measurement due to the limitation of appropriate instrumentations, field conditions and large
36 cost. In past decades, laboratory experiment is one of the main tools to investigate the
37 flow-vegetation interaction. Nepf ^[3] provided excellent results on flow structures of flow
38 through emergent vegetation. The drag force induced by vegetation was investigated. Carollo
39 *et al* ^[4] measured the local flow velocities for different vegetation densities, flow discharges,
40 and flume bed slopes using two-dimensional (2D) acoustic Doppler velocimeter (ADV). Based
41 on their experiment measurements and the *H*-theorem analysis, Carollo *et al* ^[5] proposed an
42 equation to estimate the flow resistance in vegetated open channel. Liu *et al.* ⁶ and Shan *et al.* ⁷
43 analyzed the flow direction along meandering compound channel. Wilson *et al* ^[8] investigated
44 the flow structure in open channel flow for various submerged flexible vegetation. Järvelä ^[9]
45 investigated the impact of the submerged flexible vegetation on the flow structure and flow
46 resistance using flume experiment. Folkard ^[10] conducted laboratory experiment to investigate
47 the flow within gaps in canopies of flexible, submerged aquatic vegetation. Ricardo *et al* ^[11]
48 calculated the time and space averaged flow variables in a flume with non-uniform emergent
49 vegetation from instantaneous velocity maps measured by using the particle image velocimeter
50 (PIV). Liu *et al.* ^[12] investigated the flow features in meandering compound channel with grass
51 on the floodplain. The effect of vegetation on sediment transport and deposition was examined
52 by Liu and Nepf ^[12]. More laboratory experimental studies of flow vegetation interaction can
53 be found in the recent excellent review of Nepf ^[14,15].

54 With the rapid development of computer technology and computational fluid dynamics
55 techniques, various numerical models have been developed to simulate the flow characteristics
56 in rivers and open channels. Wilson *et al* ^[16] studied the hydraulic impact of willow stands on

57 the velocity distribution using a three-dimensional (3D) standard $k-\varepsilon$ turbulence model. Guo *et*
58 *al*^[17] investigated the effect of the bed roughness on the flow structure in open channel using a
59 2D numerical model. Jing *et al*^[18,19,20] applied a 2D flow turbulence model to investigate the
60 characteristics of the water flow in meandering compound channels. Coupled with the
61 sediment transport model, they simulated the hydrodynamics and sediment transport in the
62 upper meandering reach of the Yellow River^[21]. Huai *et al.*^[22] applied layer approach to
63 simulate the flow velocity field in vegetated open channel flows by considering the effect of
64 bed roughness. Huai *et al*^[23] presented results from large eddy simulation (LES) of open
65 channel flows with non-submerged vegetation. The effect of turbulent structure on the
66 momentum transfer across the outer line of emergent vegetation patch is evaluated by Huai *et*
67 *al*^[24]. Marsooli and Wu^[25] examined the wave attenuation by vegetation using a 3D
68 Reynolds-averaged Navier–Stokes equations (RANS) model. Kim *et al*^[26] computed the flow
69 and bed morphodynamics through rigid, emergent cylinders by employing a 3D LES approach.
70 Though these studies have demonstrated many flow features in a vegetated open channel or
71 river flow, the complicated boundary condition of flow in vegetated rivers or open channels
72 still poses challenges and makes it difficult for accurate simulation on the macro level. The
73 lattice Boltzmann method (LBM), a mesoscopic method has great advantage to treat complex
74 boundary condition and is suitable for describing the internal interactions among fluid particles
75 and those between the fluid and external environment^[27,28]. As a result, LBM has been used to
76 simulate various complicated flow phenomenon, such as multiphase flows, flows in porous
77 media, quasi Newtonian fluid and chemical reaction flow^[29-31].
78 In recent years, LBM has been applied to simulate open channel flow with vegetation.
79 Jimenez-Hornero *et al* developed a two-dimensional lattice model to describe the influence of
80 vegetation on the turbulent flow structure in an open channel^[32]. Yang *et al* developed a
81 two-dimensional lattice Boltzmann model with a D2Q9 lattice arrangement to simulate the
82 flow-vegetation interactions in an open channel^[33]. Buxon studied the fluid dynamics of acid
83 mine drainage flow using a lattice Boltzmann model with a D2Q9 lattice arrangement^[34].
84 In this study, the LBM is applied to simulate the flow structure in a laboratory flume with rigid
85 vegetation for a range of flow conditions and vegetation arrangements. The multi-relaxation

86 time lattice Boltzmann equation (MRT-LBE) model is proposed with the specific numerical
 87 algorithm to treat the instability of the single-relaxation time (SRT) model for flows with large
 88 Reynolds number. To improve the simulation accuracy, the drag force induced by vegetation is
 89 considered in the model to take into account of the effect of vegetation on the flow field.
 90 Accompanied laboratory experiments have been carried out in a flume with vegetation to
 91 validate the numerical simulation. Three-dimensional laser Doppler velocimeter (3D LDV) is
 92 used to measure the flow velocity field.

93

94 **2. Mathematical model and numerical algorithm**

95 The Boltzmann equation that describes the spatial and temporal distribution of particle
 96 velocities is a very complex integral differential equation, which is difficult to obtain its
 97 analytic solutions^[35,36] and has to be solved numerically. The LBM is the spatial, temporal,
 98 and velocity space discretized formation for Boltzmann equation, and consists of three
 99 components: the evolution equation of distribution function, the discrete velocity model and
 100 the equilibrium distribution function. In addition, the boundary conditions have to be specified
 101 to solve the equations.

102

103 **2.1 The evolution equation of distribution function**

104 The evolution equation of particle distribution function is the lattice Boltzmann equation (LBE)
 105 and can be written as^[36]:

$$106 \quad f_i(\mathbf{x} + \mathbf{c}_i \Delta t, t + \Delta t) = f_i(\mathbf{x}, t) + \Omega_i(f), i = 0, 1, 2, \dots, b-1 \quad (1)$$

107 where $f_i(\mathbf{x}, t)$ = the i^{th} particle distribution function, b = the number of discrete velocities, \mathbf{c}_i =
 108 the i^{th} particle velocity, Δt = the time step, $\Omega_i(f)$ = the collision operator, which reflects the
 109 variation of the distribution function caused by collision.

110 It is difficult to solve the LBE due to the complexity of the collision term. To overcome this
 111 difficulty, Bhatnagar, Gross, and Krook simplified the equation and proposed the following
 112 lattice BGK equation (LBGK)^[37,38]:

$$113 \quad f_i(\mathbf{x} + \mathbf{c}_i \Delta t, t + \Delta t) = f_i(\mathbf{x}, t) - \frac{1}{\tau} \left(f_i(\mathbf{x}, t) - f_i^{eq}(\mathbf{x}, t) \right) \quad (2)$$

114 where τ = the relaxation time, and $f_i^{eq}(\mathbf{x}, t)$ = the local equilibrium distribution function. In

115 SRT model, the following equilibrium distribution function is adopted^[39]:

116

$$f_i^{eq}(\mathbf{x}, t) = w_i \rho \left[1 + \frac{\mathbf{c}_i \cdot \mathbf{u}}{c_s^2} + \frac{(\mathbf{c}_i \cdot \mathbf{u})^2}{2c_s^4} - \frac{\mathbf{u} \cdot \mathbf{u}}{2c_s^2} \right] \quad (3)$$

117

where w_i = weight coefficient, ρ = the fluid density, \mathbf{u} = the macro fluid velocity, c_s = the grid sound speed.

119

120 *The discrete velocity model*

121

Among the LBGK models, the widely used one is *DnQb* models developed by Qian, *et al.* [39], where n is the space dimension, and b is the number of discrete velocities. In this study,

122

123

D2Q9 model is used, where the discrete velocity vectors are organized as following matrix:

124

$$\mathbf{c} = [c_0, c_1, \dots, c_8] = c \begin{bmatrix} 0 & 1 & 0 & -1 & 0 & 1 & -1 & -1 & 1 \\ 0 & 0 & 1 & 0 & -1 & 1 & 1 & -1 & -1 \end{bmatrix} \quad (4)$$

125

in which $c = \Delta x / \Delta t$, Δx = the spatial step.

126

127

In the model, the grid sound speed and the weight factors for corresponding distribution functions are taken as follows:

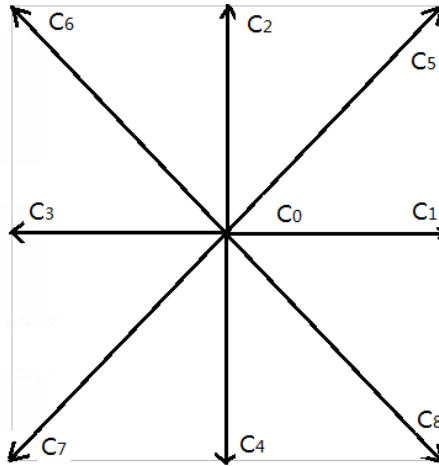
128

129

$$c_s = \frac{c}{\sqrt{3}}, \quad w_0 = \frac{4}{9}, \quad w_{1-4} = \frac{1}{9}, \quad w_{5-8} = \frac{1}{36}.$$

130

The discrete velocities and their weight factors in the D2Q9 model are shown in Fig.1.



131

132

Fig. 1. The discrete velocities and their weight factors in the D2Q9 model

133

134 *2.2 The MRT-LBE model*

135

In the LBGK model, the collision operator is linearized and the computational process of LBE has been simplified. However, the application of the LBGK model is limited because of only single relaxation time is used. d'Humeriers proposed a generalized LBE (GLBE) model, which is named as multiple-relaxation-time lattice Boltzmann equation (MRT-LBE) model [35,40].

138

139
$$f_i(\mathbf{x} + \mathbf{c}_i \Delta t, t + \Delta t) - f_i(\mathbf{x}, t) = - \sum_{j=0}^{b-1} \Lambda_{ij} [f_j(\mathbf{x}, t) - f_j^{eq}(\mathbf{x}, t)], \quad i = 0, 1, \dots, b-1 \quad (5)$$

140 where Λ_{ij} is the element of matrix Λ , and $-\Lambda = [-\Lambda_{ij}]_{b \times b}$ is named as collision matrix.

141 The collision step of the MRT-LBE in the velocity space is difficult to perform, and needs to
 142 be transformed. Let S be a diagonal matrix and the relationship between S and Λ be as
 143 following:

144
$$\mathbf{S} = \mathbf{M} \mathbf{A} \mathbf{M}^{-1} = \text{diag}(s_0, s_1, \dots, s_{b-1}), \quad (6)$$

145 in which \mathbf{M} is called the transformation matrix. Equation (5) can then be rewritten in vector
 146 form as following:

147
$$\mathbf{f}(\mathbf{x} + \mathbf{c}_i \Delta t, t + \Delta t) - \mathbf{f}(\mathbf{x}, t) = -\mathbf{A}[\mathbf{f}(\mathbf{x}, t) - \mathbf{f}^{eq}(\mathbf{x}, t)] \quad (7)$$

148 where $\mathbf{f} = (f_0(x, t), f_1(x, t), \dots, f_{b-1}(x, t))^T$.

149 Define \mathbf{p} as:

150
$$\mathbf{p} = \mathbf{M} \mathbf{f} = [p_0, p_1, \dots, p_{b-1}]^T, \quad (8)$$

151 The following equation can be obtained by pre-multiplying matrix \mathbf{M} to the both sides of (7):

152
$$\mathbf{p}(\mathbf{x} + \mathbf{c}_i \Delta t, t + \Delta t) - \mathbf{p}(\mathbf{x}, t) = -\mathbf{S}[\mathbf{p}(\mathbf{x}, t) - \mathbf{p}^{eq}(\mathbf{x}, t)] \quad (9)$$

153 Therefore, the component-wise of (9) can be written as:

154
$$p_i(\mathbf{x} + \mathbf{c}_i \Delta t, t + \Delta t) - p_i(\mathbf{x}, t) = -s_i [p_i(\mathbf{x}, t) - p_i^{eq}(\mathbf{x}, t)], \quad i = 0, \dots, b-1 \quad (10)$$

155 As such, \mathbf{p} can be calculated with the similar steps of the LBGK model, and \mathbf{f} can then be
 156 calculated by the following transformation:

157
$$\mathbf{f} = \mathbf{M}^{-1} \mathbf{p} \quad (11)$$

158 For the convenience of numerical simulation, pre-multiplying (9) with \mathbf{M}^{-1} yields:

159
$$\mathbf{f}(\mathbf{x} + \mathbf{c}_i \Delta t, t + \Delta t) - \mathbf{f}(\mathbf{x}, t) = -\mathbf{M}^{-1} \mathbf{S}[\mathbf{p}(\mathbf{x}, t) - \mathbf{p}^{eq}(\mathbf{x}, t)] \quad (12)$$

160 The above equation can be divided into the collision step and the migration step. The collision
 161 step can be calculated as:

162
$$\tilde{\mathbf{f}}(\mathbf{x}, t) = \mathbf{f}(\mathbf{x}, t) - \mathbf{M}^{-1} \mathbf{S}[\mathbf{p}(\mathbf{x}, t) - \mathbf{p}^{eq}(\mathbf{x}, t)] \quad (13)$$

163 where $\tilde{\mathbf{f}}(\mathbf{x}, t)$ is distribution functions immediately after the collision, and the migration
 164 step is:

165
$$\mathbf{f}(\mathbf{x} + \mathbf{c}_i \Delta t, t + \Delta t) = \tilde{\mathbf{f}}(\mathbf{x}, t) \quad (14)$$

166 In the MRT-LBE model, the transformation matrix and the diagonal matrix for D2Q9 are^[38]:

$$\mathbf{M} = \begin{pmatrix} 1 & 1 & 1 & 1 & 1 & 1 & 1 & 1 & 1 \\ -4 & -1 & -1 & -1 & -1 & 2 & 2 & 2 & 2 \\ 4 & -2 & -2 & -2 & -2 & 1 & 1 & 1 & 1 \\ 0 & 1 & 0 & -1 & 0 & 1 & -1 & -1 & 1 \\ 0 & -2 & 0 & 2 & 0 & 1 & -1 & -1 & 1 \\ 0 & 0 & 1 & 0 & -1 & 1 & 1 & -1 & -1 \\ 0 & 0 & -2 & 0 & 2 & 1 & 1 & -1 & -1 \\ 0 & 1 & -1 & 1 & -1 & 0 & 0 & 0 & 0 \\ 0 & 0 & 0 & 0 & 0 & 1 & -1 & 1 & -1 \end{pmatrix} \quad (15)$$

168

and

$$\mathbf{S} = \text{diag}(1, 1.4, 1.4, 1.0, 1.2, 1.0, 1.2, 2/(1+6\nu), 2/(1+6\nu))^T \quad (16)$$

170

where ν = fluid viscosity, and the vector \mathbf{p} is defined as:

$$\mathbf{p} = (\rho, e, \varepsilon, j_x, q_x, j_y, q_y, p_{xx}, p_{xy})^T \quad (17)$$

172

The equilibrium state vector of \mathbf{p} is:

$$\mathbf{p}^{eq} = (\rho, -2\rho + 3(j_x^2 + j_y^2), \rho - 3(j_x^2 + j_y^2)^2, j_x, -j_x, j_y, -j_y, j_x^2 - j_y^2, j_x j_y)^T \quad (18)$$

174

in which

$$j_x = \rho u_x = \sum_i f_i c_{ix} - F_x \Delta t, \quad j_y = \rho u_y = \sum_i f_i c_{iy} - F_y \Delta t. \quad (19)$$

176

where $\mathbf{F} = (F_x, F_y)^T$ = the external force.

177

178 **2.3 The drag force of vegetation**

179

180 Drag force induced by aquatic vegetation has great impact to water flow. Therefore, it is
181 important to consider the aquatic vegetation induced drag force in the mathematical model. In
182 this study, vegetation-induced drag force is considered in the MRT-LBE model, and based on
183 the research result in [41-43], the drag force of the vegetation in the two dimensional MRT-
LBE model (D2Q9) can be estimated as:

$$\mathbf{F}_D = \left(\frac{1}{2} \rho m \beta C_D D U u_x, \frac{1}{2} \rho m \beta C_D D U u_y \right) \quad (20)$$

185

where m = the vegetation numbers per unit area; ρ = water density; β = the constant related

186

to the vegetation type, C_D = the drag force coefficient, D = the vegetation diameter,

187 $U = \sqrt{u_x^2 + u_y^2}$. $\beta = 1$ when the vegetation is regular, and $C_D = 1$ when the Reynolds
 188 number of the vegetation ranges from 1000 to 10000.

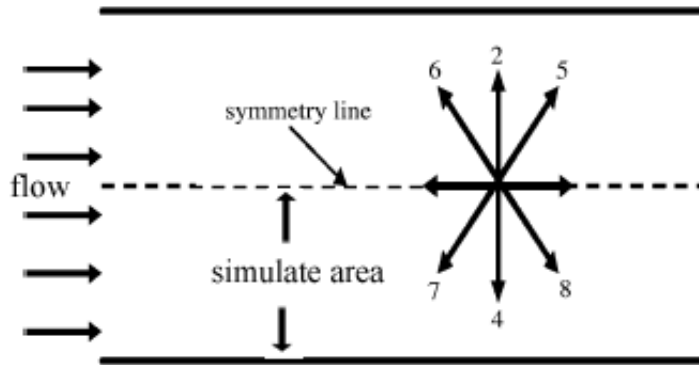
189 Following three methods are usually adopted in the LBGK model to consider the effect of
 190 external force ^[35]: the pressure correction in the equilibrium distribution function, the velocity
 191 correction in the equilibrium distribution, and the extra force term in the evolution equation.
 192 Among these methods, the second method is relatively easy to implement to and easy to
 193 generalize in the MRT-LBE model, in which the drag forces are included. Therefore, j_x and j_y
 194 in the equilibrium distribution function in (18) are calculated as following:

195
$$j_x = \rho u_x = \sum_i f_i c_{ix} - \frac{1}{2} \rho m \beta C_D D U u_x, \quad j_y = \rho u_y = \sum_i f_i c_{iy} - \frac{1}{2} \rho m \beta C_D D U u_y \quad (21)$$

196

197 **2.4 Boundary conditions**

198 The laboratory flume is symmetric about the center line of the flume, and the vegetation group
 199 is symmetric about the center line. Therefore, in order to save the simulation time, only the
 200 flow region from the left wall to the center line of the flume is simulated in the numerical
 201 computation. As a result, the symmetric boundary condition is adopted at the center line, as
 202 shown in Fig. 2.



203

204 Fig. 2. The symmetry boundary condition of D2Q9

205 If the simulated area is from the south wall to the center line, then the unknown distribution
 206 functions (f_4 , f_7 and f_8) at the center line can be calculated as follows:

207
$$f_4 = f_2, f_8 = f_5, f_7 = f_6. \quad (22)$$

208

209 At the inlet boundary (west), the flow velocity is known, and the following conditions can be
 210 derived ^[38]:

211
$$\rho_w = \frac{1}{1-u_w} (f_0 + f_2 + f_4 + 2(f_3 + f_6 + f_7)), \quad (23)$$

212
$$f_1 = f_3 + \frac{2}{3} \rho_w u_w, \quad (24)$$

213
$$f_5 = f_7 - \frac{1}{2} (f_2 - f_4) + \frac{1}{6} \rho_w u_w + \frac{1}{2} \rho_w v_w, \quad (25)$$

214
$$f_8 = f_6 + \frac{1}{2} (f_2 - f_4) + \frac{1}{6} \rho_w u_w - \frac{1}{2} \rho_w v_w. \quad (26)$$

215 where u_w = the velocity at the inlet, and it is given in a parabolic distribution along the
216 cross-section:

217
$$u_w = 4u_{\max} \left(\frac{y}{B} - \frac{y^2}{B^2} \right) \quad (27)$$

218 In which, u_{\max} = the maximum velocity at the inlet; B = the width of the channel; y = the
219 transverse distance from the left bank of the channel.

220

221 At the outlet boundary (east), the following full development boundary condition is used:

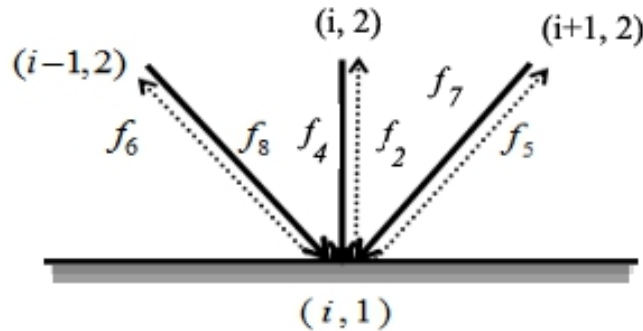
222
$$f_{k,n} = f_{k,n-1}, k = 0, \dots, 8. \quad (28)$$

223 At the solid wall boundary (south boundaries and the vegetation), the bounce back boundary
224 condition is applied ^[36], as shown in Fig. 3. For example, at the south wall, the unknown

225 distribution functions f_5, f_2, f_6 can be obtained as $f_5 = f_7, f_2 = f_4, f_6 = f_8$, in which

226 f_7, f_4, f_8 at the node $(1,1)$ can be calculated by migrating the neighbor nodes, i.e.

227 $f_7(i,1) = f_7(i+1,2), f_4(i,1) = f_4(i,2), f_8(i,1) = f_8(i-1,2).$



228

229

Fig. 3. The bound back condition at south wall

230

231

2.5 The algorithm of MRT-LBE with drag force induced by vegetation

232 It is important to design an algorithm of the MRT-LBE model that can consider the influence
233 of the vegetation-induced drag force on the flow structure in order to improve the accuracy of
234 the numerical simulation. The algorithm of the MRT-LBE model with drag force induced by
235 vegetation can be described as follows.

236 **Step 1. Mesh generation**

237 As the computational domain is rectangular, the square grids are used to divide the domain and
238 the spatial and computational time steps are set as unit ($=1$).

239 **Step 2. Initial conditions**

240 The initial velocities, density and distribution functions are specified as following:

241 Velocities at x and y directions (u_x and u_y) are set as zero at all grids except for inlet grids; the
242 initial density ($\rho = 1$) is set as 1; the initial distribution function is set as

243 $f_i = w_i \rho, i = 0, 1, L, b-1$, where w_i is the weighting factor along the i -th direction.

244 **Step 3. Calculation of $\mathbf{p}^{\text{eq}}(\mathbf{x}, t)$ and $\mathbf{p}(\mathbf{x}, t)$**

245 $\mathbf{p}^{\text{eq}}(\mathbf{x}, t)$ can be calculated according to (18) and $\mathbf{p}(\mathbf{x}, t)$ is obtained from (8).

246 **Step 4. Collision step**

247 The distribution function after collision ($\tilde{\mathbf{f}}(\mathbf{x}, t)$) is calculated by (13).

248 **Step 5. Migration step**

249 The distribution function of the next time step ($\mathbf{f}(\mathbf{x} + \mathbf{c}\Delta t, t + \Delta t)$) is calculated by (14).

250 **Step 6. Boundary conditions**

251 At the inlet, u_w and v_w are specified, ρ_w and unknown distribution functions are calculated
252 by (23)-(26). At the outlet, full development boundary condition is used, and the unknown
253 distribution functions can be calculated by (28). At the solid wall (solid boundary of the flume
254 and the vegetation), bounce back boundary condition is applied. At the center line of the flume,
255 the symmetry boundary condition is adopted and the unknown distribution functions can be get
256 by (22).

257 **Step 7. Calculation of macroscopic physical quantities**

258 The macroscopic physical quantities can be calculated as follows after distribution functions
 259 have been obtained:

$$260 \quad \rho = \sum_{i=0}^{b-1} f_i, \quad u_x = \frac{1}{\rho} \sum_{i=0}^{b-1} f_i c_{ix}, \quad u_y = \frac{1}{\rho} \sum_{i=0}^{b-1} f_i c_{iy} \quad (29)$$

261 Steps 3 - 7 are repeated until a prescribed time step is reached.

262

263 **3. Description of experiment and numerical simulation**

264 **3.1 Description of laboratory experiment**

265 In order to validate the numerically simulated results, physical laboratory experiments have
 266 been carried out using a flume, which is 15m length, 0.49m width and 0.5m depth. The 3D
 267 LDV is used to measure the flow velocity field. Glass rods with three diameters of $D=10\text{mm}$,
 268 8mm and 6mm and the height of 0.5m are used to simulate unsubmerged vegetation in
 269 experiments. Because the flow characteristics of vegetation with different diameters is similar,
 270 only the measured results with rod diameter of 10mm are presented and discussed in this
 271 paper.

272 Four typical cases are chosen for experiments with different vegetation arrangements, as listed
 273 in Table 1 in which the flow Reynolds number and the vegetation Reynolds number are
 274 calculated as follows:

$$275 \quad \text{Re}_w = U_{in} R_{ih} / \nu \quad (30)$$

$$276 \quad \text{Re}_v = U_{in} D / \nu \quad (31)$$

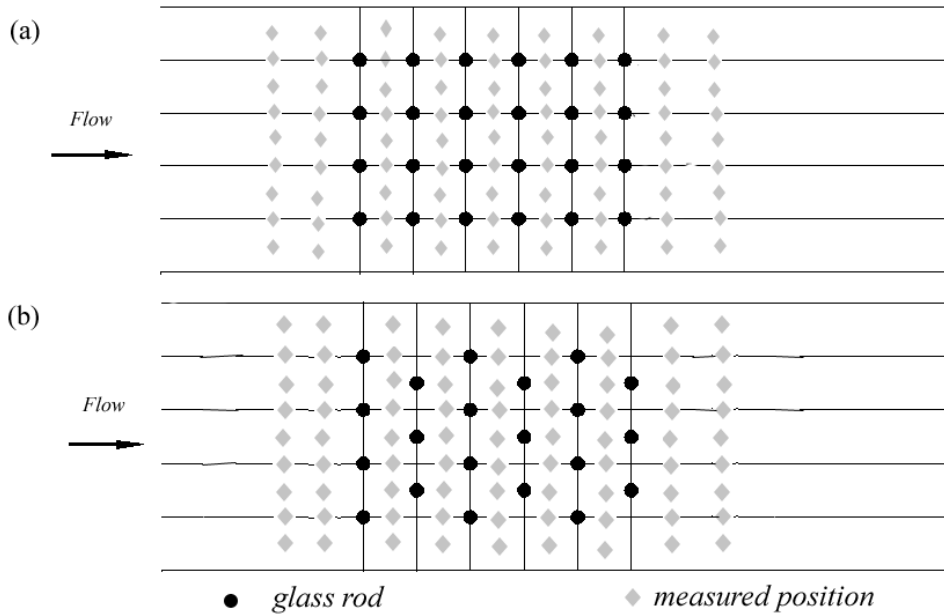
277 where U_{in}, R_{ih} are the averaged flow velocity and hydraulic radius at the flow inlet,
 278 respectively; ν is the water viscosity coefficient. Water flow discharge is kept as $0.054\text{m}^3/\text{s}$
 279 for all the four cases.

280 Table 1. Basic conditions of the four typical cases

Case	Vegetation's arrangement	Water depth /m	Hydraulic radius /m	Inlet velocity /m/s	Vegetation Number	Flow Reynolds number	Vegetation Reynolds number
1	Sparse and staggered	0.206	0.112	0.529	38	59199	5296
2	Dense and staggered	0.254	0.125	0.430	149	53625	4300
3	Sparse and parallel	0.189	0.107	0.577	35	61562	5772
4	Dense and parallel	0.235	0.120	0.464	143	55656	4642

281

282 The first row of glass rods was arranged 8.48m from the inlet of the flume. The row and
 283 column numbers of the rods for dense conditions were 11 and 13, respectively; while for
 284 sparse conditions, they were 5 and 7, respectively. Both the longitudinal and transverse
 285 distances between two neighbor rods were 81.7mm for Cases 1 and 3, and were 40.8mm for
 286 Cases 2 and 4. The length of the vegetation area was 0.49 m for all the four cases. The position
 287 of the glass rods was shown in Fig. 4.



288

289

Fig. 4. Sketch of the rods and measured position

290

291

292

293

294

295

296

3.2 Description of the simulated area and mesh generation

297

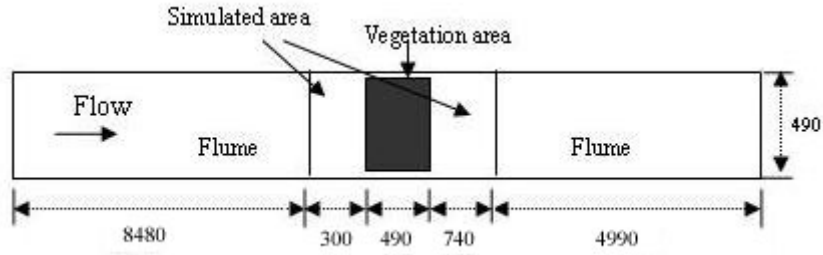
298

299

300

301

It would be expensive and unnecessary to set the whole flume as computational domain. As one is only interested in the flow characteristics around the vegetation patch, a region of 1.53m×0.49m, covering the vegetation patch, is chosen as the computational domain. The domain is 8.48m from the inlet of the flume. The vegetation patch is 0.49m long and 0.49m wide, as shown in Fig. 5.



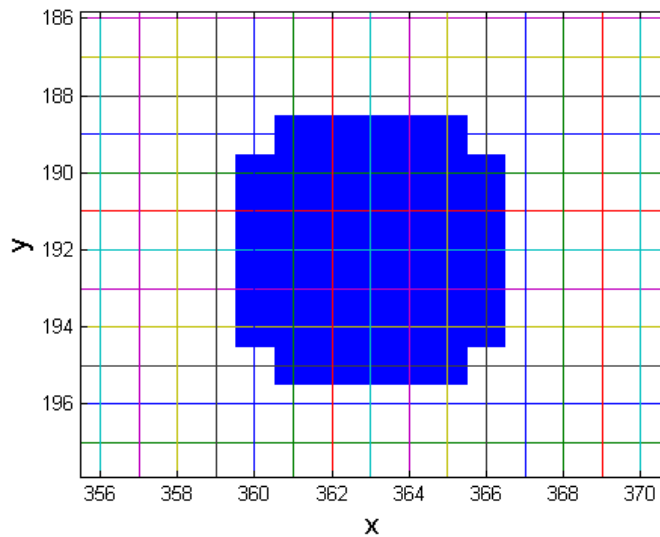
302

303 Fig. 5. Sketch of simulated area and vegetation area in the laboratory flume (unit: mm)

304

305 The simulated area is a rectangle with 1.53m long (in the x-direction) and 0.49m wide (in the
 306 y-direction). Because the flume and the flow condition are symmetry along the y-direction,
 307 only a half of the area is used for numerical simulation. So the actual simulated area is 1.53m
 308 long in the x-direction and 0.245m wide in the y-direction.

309 1200 grids and 192 grids are assigned along the x- and y- directions, respectively. There are
 310 $1200 \times 192 = 230400$ grid cells for the whole simulated area. Each of the glass rods are
 311 covered by 7.8 grids along both the x- and y- directions, as shown in Fig. 6.



312

313 Fig. 6. The mesh around a typical glass rod

314

4. Results and discussion

315

4.1 Evaluation of numerical convergence

316

To investigate the convergence of the MRT-LBE numerical model, numerical tests have been
 317 carried out with three different grid resolutions for Case 1. These runs have grid numbers of

318 $N=600 \times 192$, 1200×384 and 2400×768 , respectively, these grids correspond respectively to
 319 the vegetation spacing of 40.85, 81.7 and 163.4 mm, In order to estimate the convergence, the
 320 numerical error of any run (E) is assumed to be proportional to l^n , where l is the mesh size, and
 321 n is the order of the convergence^[44]. Letting E_N and l_N denote the numerical error and mesh
 322 size with grid numbers of N , respectively, then

$$323 \quad E_N \approx \alpha(l_N)^n$$

324 Where α is a constant. It is noticed that $l_{600 \times 192} = 2l_{1200 \times 384} = 4l_{2400 \times 768}$, and as a result, the
 325 following formula can be obtained.

$$326 \quad \frac{E_{600 \times 192} - E_{1200 \times 384}}{E_{1200 \times 384} - E_{2400 \times 768}} \approx \frac{(l_{600 \times 192})^n - (l_{1200 \times 384})^n}{(l_{1200 \times 384})^n - (l_{2400 \times 768})^n} = \frac{(2l_{1200 \times 384})^n - (l_{1200 \times 384})^n}{(l_{1200 \times 384})^n - (\frac{1}{2}l_{1200 \times 384})^n}$$

$$= \frac{2^n - 1}{1 - 2^{-n}} = 2^n$$

327 An averaged value of the left hand side of above formula is 3.3. Therefore, the order of
 328 convergence for the numerical method is about 1.7.

329

330 **4.2 Comparison between simulated and measured data**

331 Before simulation using the LBM, it is usually to transform all the physical variables into
 332 non-dimensional form (lattice units)^[38]. Let ρ_P , L_P , W_P , D_P , U_P , Re_P , ν_P , F_P and ρ_L , L_L , W_L , D_L ,
 333 U_L , Re_L , ν_L , F_L be the density of water, length of the flume, width of the flume, diameter of the
 334 rods, flow velocity, Reynolds number, fluid kinematic viscosity and drag force of vegetation in
 335 the physical area and the computational domain, respectively, then these variables must satisfy
 336 the following relationships:

$$337 \quad \frac{L_P}{L_L} = \frac{W_P}{W_L} = \frac{D_P}{D_L} \quad (32)$$

$$338 \quad Re_P = \frac{U_P D_P}{\nu_P} = \frac{U_L D_L}{\nu_L} = Re_L \quad (33)$$

$$339 \quad \frac{F_P}{F_L} = \frac{\rho_P}{\rho_L} \left(\frac{D_L}{D_P} \right)^2 \left(\frac{\mu_P}{\nu_L} \right)^2 \quad (34)$$

340 Equations (32) and (33) indicate that the non-dimensional form of the basic parameters in the

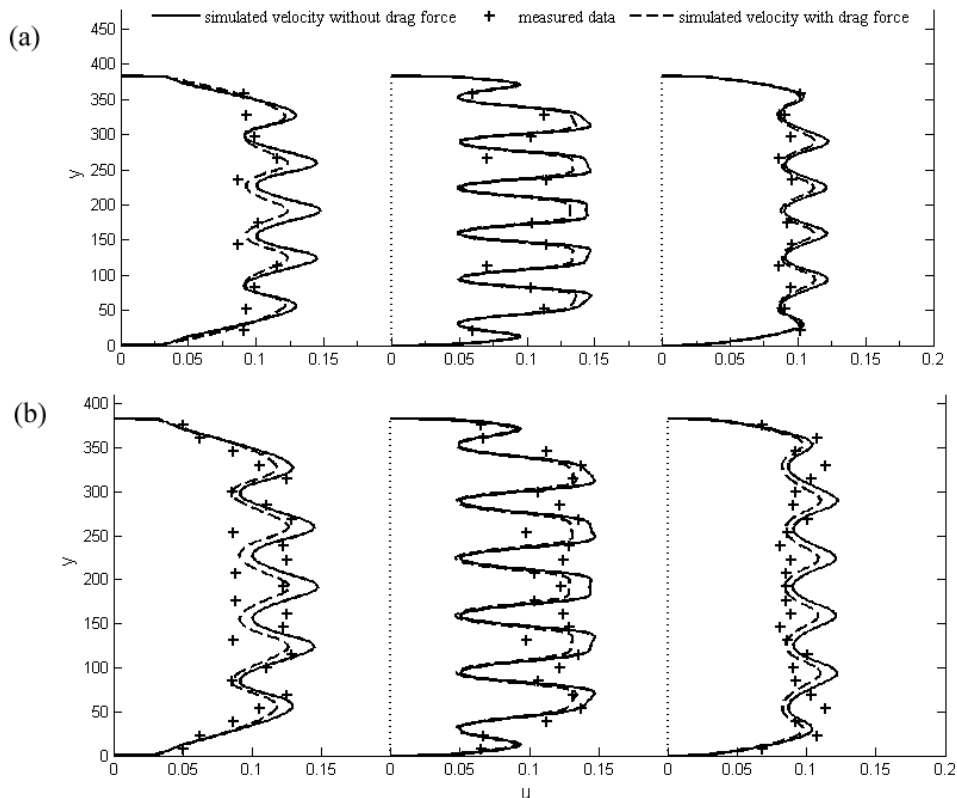
341 computational domain are calculated, as shown in Table 2. For the convenience of comparison,
 342 the dimensional basic parameters are also presented.

343

344 Table 2. Basic parameters in dimensional and non-dimensional forms

Cases	Dimensional form					Non-dimensional form				
	U_{in} /m/s	L /m	W /m	D /m	ν m ² /s	U_{in}	L	W	D	ν
1	0.529	1.53	0.49	0.01	1.31E-06	0.20	1200	384	7.84	0.00039
2	0.430	1.53	0.49	0.01	1.31E-06	0.16	1200	384	7.84	0.00038
3	0.577	1.53	0.49	0.01	1.31E-06	0.22	1200	384	7.84	0.00039
4	0.464	1.53	0.49	0.01	1.31E-06	0.18	1200	384	7.84	0.00040

345 In order to investigate the effect of vegetation on flow structure, two simulations have been
 346 performed with one considering the vegetation-induced drag force and another without
 347 considering the drag force generated by vegetation. For convenient comparison, the measured
 348 velocity is converted into non-dimension form as shown in Fig. 7.



349

350 Fig. 7. Comparison between the simulated and measured velocities (a) Case 1; (b) Case 2

351 Three cross sections (3 lines perpendicular to the banks of the channel) at the middle of two

352 adjacent columns of vegetation are chosen for comparison. The distances of these sections
353 from the inlet are 347, 443 and 539, respectively.

354 Fig. 7 shows that the simulated flow velocity decreases when the drag force generated by
355 vegetation is considered. It is seen that the simulated velocity with vegetation-induced drag
356 force agrees well with the laboratory measurements, while there exists some discrepancy
357 between the simulation and measurement when the drag force generated by vegetation is
358 ignored in the numerical model. This indicates that the numerical simulation accuracy can be
359 improved when the vegetation-induced drag force is taken into account.

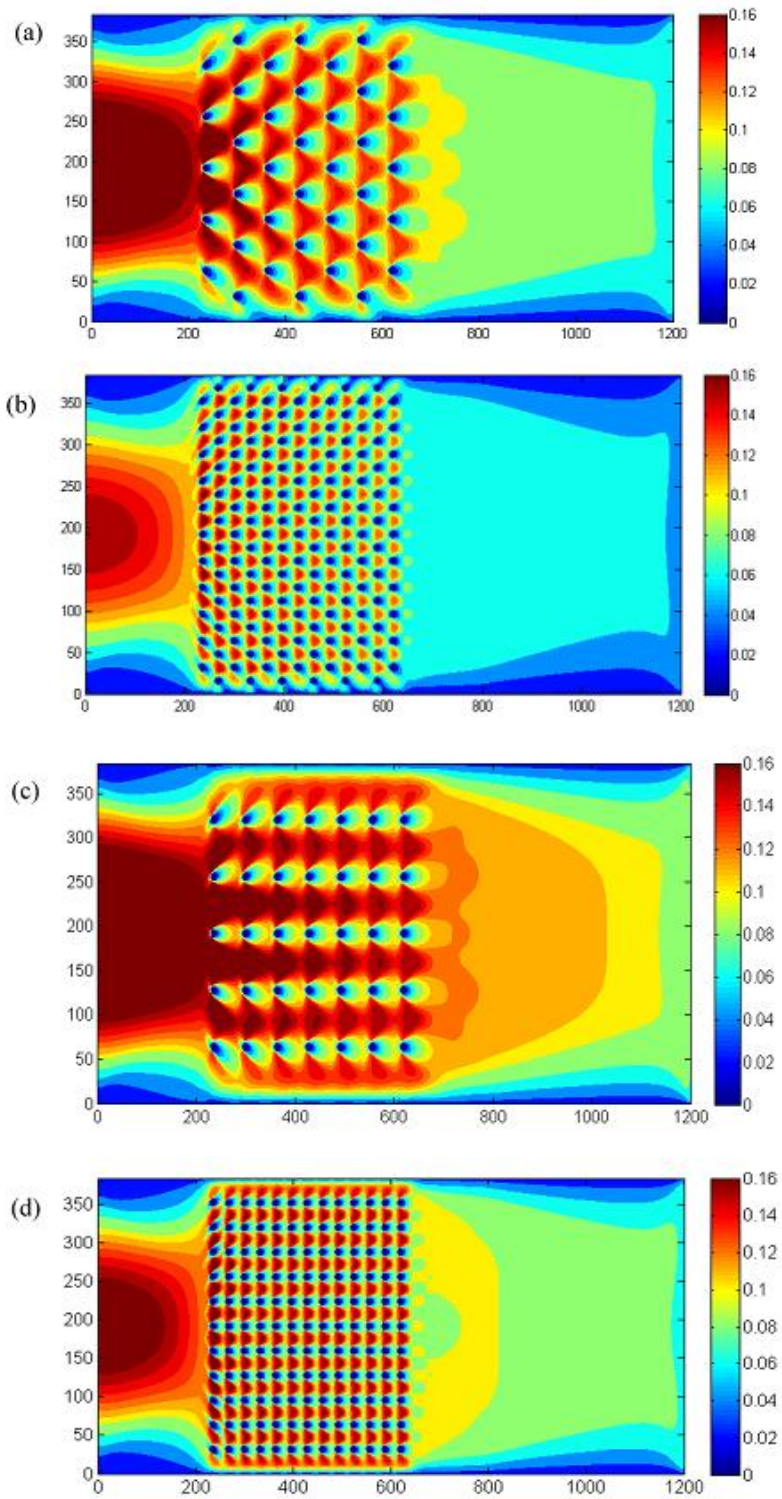
360 Figure 7 also shows that the flow velocity field is an indented distribution. The flow behind
361 glass rods is held back due to the blockage effect caused by them. As a result, the flow velocity
362 decreases greatly behind the rods. Meanwhile, the flow velocity between rods increases. A
363 little difference is found between the simulated and measured velocities. In general, the
364 simulated velocity field is in good agreement with the measured one when the
365 vegetation-induced drag force is considered.

366

367

4.3 Comparison among numerically simulated results

368 Fig. 8 shows the simulated velocity distributions for Cases 1-4. It can be found that the
369 velocity distributions largely depend on the arrangement of the rods. In the upstream of the
370 computational domain, i.e. from the inlet to the first column of the vegetation, the flow
371 velocity shows a parabolic distribution along the transverse direction for all the four cases. In
372 the vegetation area, i.e. from the first column of rods to the last column of rods, the velocity
373 distribution is very complicated. Flow velocity becomes smaller near the rods, while it is larger
374 near the middle of two adjacent rows of rods. When the rods are staggered (Cases 1 and 2), the
375 main stream lines are not parallel to the channel banks due to the complex blockage effect
376 generated by staggered rods. However, when the rods are parallel, the main stream lines are
377 approximately parallel to the channel banks. Moreover, it can be found that the velocity
378 between two adjacent rod rows is parabolic distribution along the transverse direction.



379

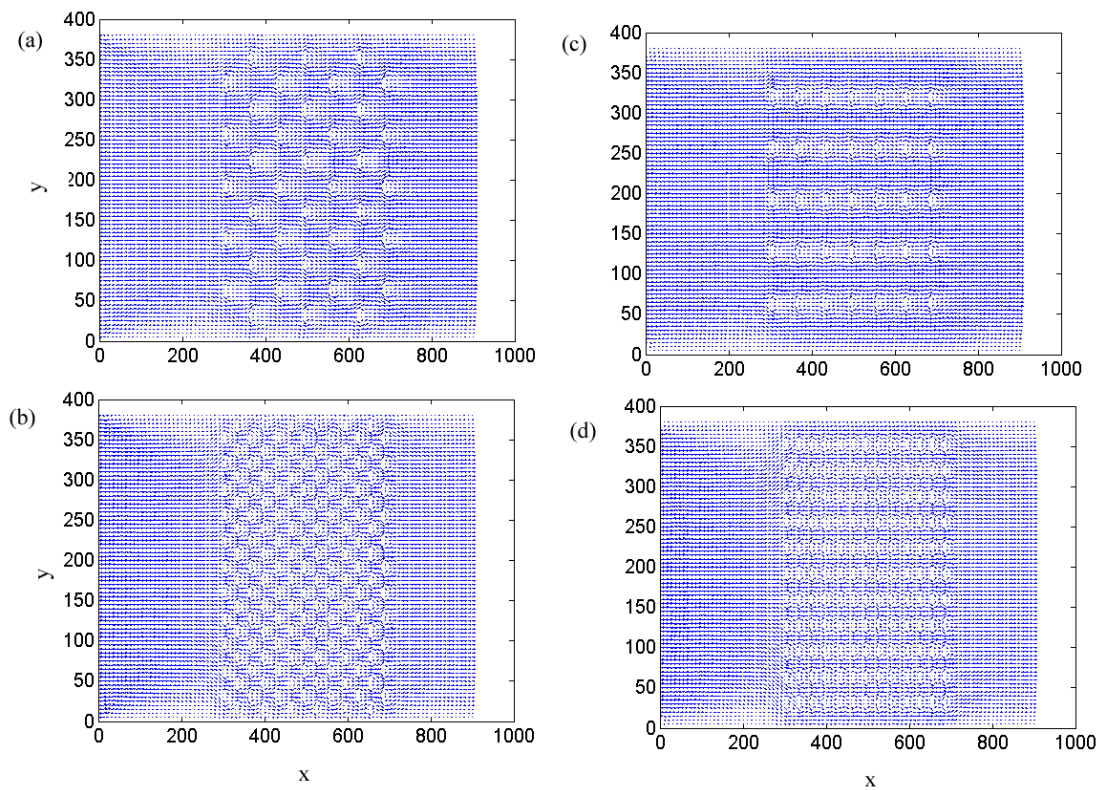
380 Fig. 8. Comparison of the flow velocity contour among four typical cases (a) Case 1; (b) Case

381 2; (c) Case 3; (d) Case 4.

382 In the downstream of the vegetation area, i.e. from the last column of vegetation to the outlet,

383 when the rods are denser and staggered (Case 2), flow velocity reaches the smallest and the

384 most uniform among the four cases. This means that such rod arrangement generates the
 385 largest blockage effect and flow resistance to water flow. Meanwhile, when the rods are sparse
 386 and parallel (Case 3), the flow velocity reaches the largest and the mostly uniform among the
 387 four cases, indicating that the smallest flow resistance is generated by such rod array.
 388 Fig. 9 is the flow velocity field within the vegetation area for all four cases to clearly show the
 389 flow characteristics. It is seen that the flow velocity field is very complex in the vegetation
 390 area, especially when the rods are staggered (Cases 1 and 2). Secondary flow circulation is
 391 seen to form close to rod when water flow passes the rod. In order to show the flow field more
 392 clearly, the flow field around some typical rods in Case 2 is enlarged, as shown by Fig. 10.

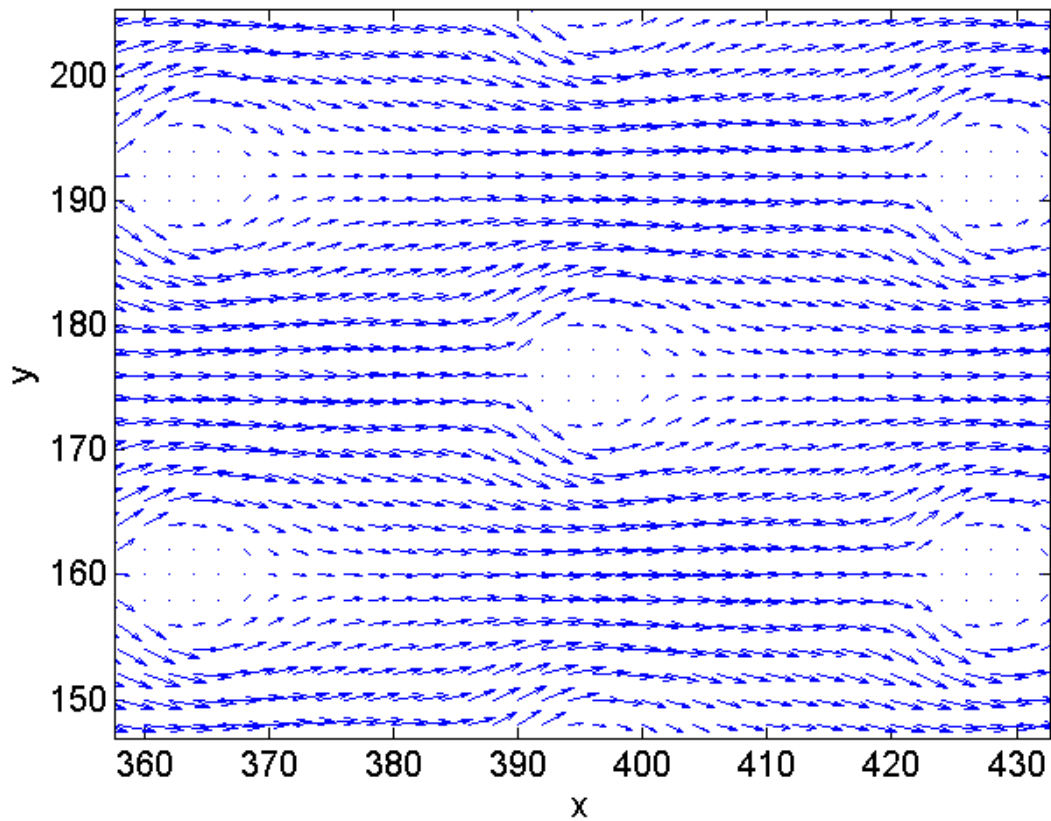


393

394 Fig. 9. Flow velocity field in the vegetation area of four cases (a) Case 1; (b) Case 2; (c)

395

Case 3; (d) Case 4



396

397

Fig. 10. Flow field around some typical rods in Case 2

398

Fig. 11 shows the flow streamlines for the four cases. It is seen that the oscillation of

399

streamlines appears when flow passes through the vegetation area. Such streamline oscillation

400

diminishes and dies out after flow exits the vegetation area. In the vegetation area, the

401

streamlines are approximately parallel to the channel banks when the rods are parallel, while

402

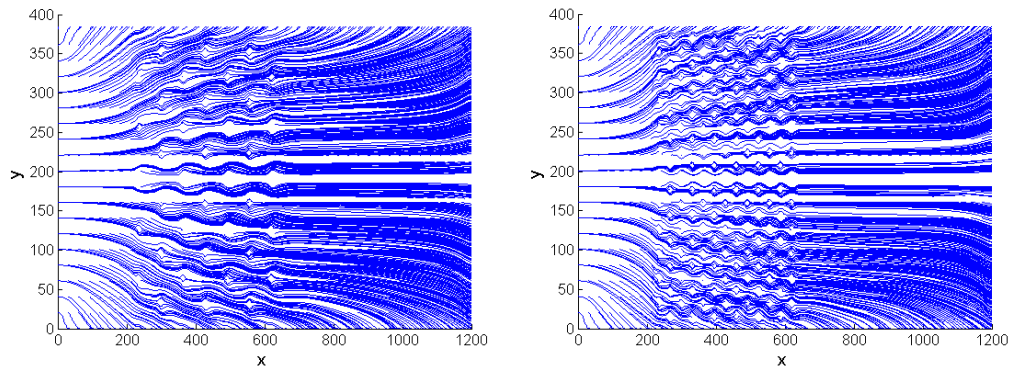
the streamlines become very complicated when the rods are staggered. In order to show the

403

streamline more clearly, the streamline around some typical rods in Case 2 is presented, as

404

shown in Fig. 12.

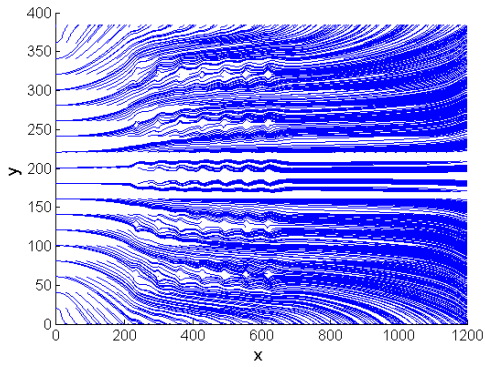


405

(a) Case 1

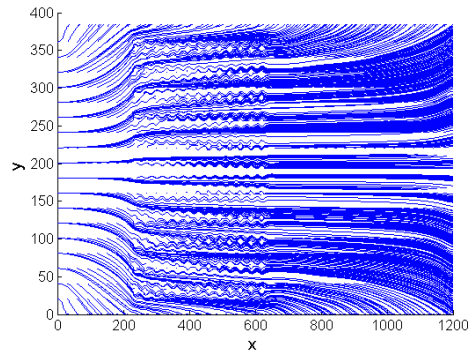
(b) Case 2

406



407

(c) Case 3

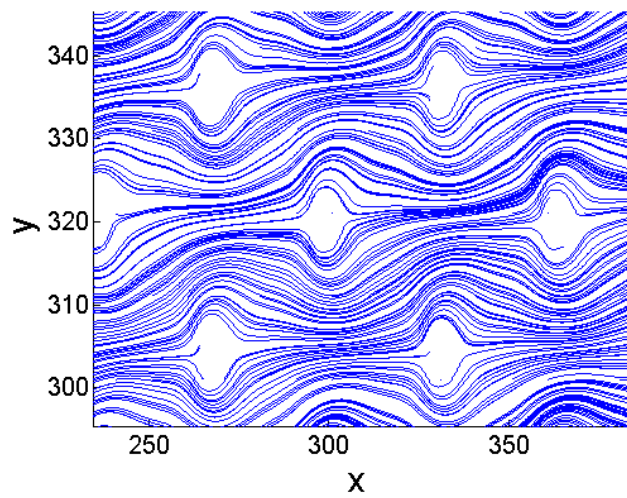


(d) Case 4

408

409

Fig. 11. Flow streamlines of four typical cases

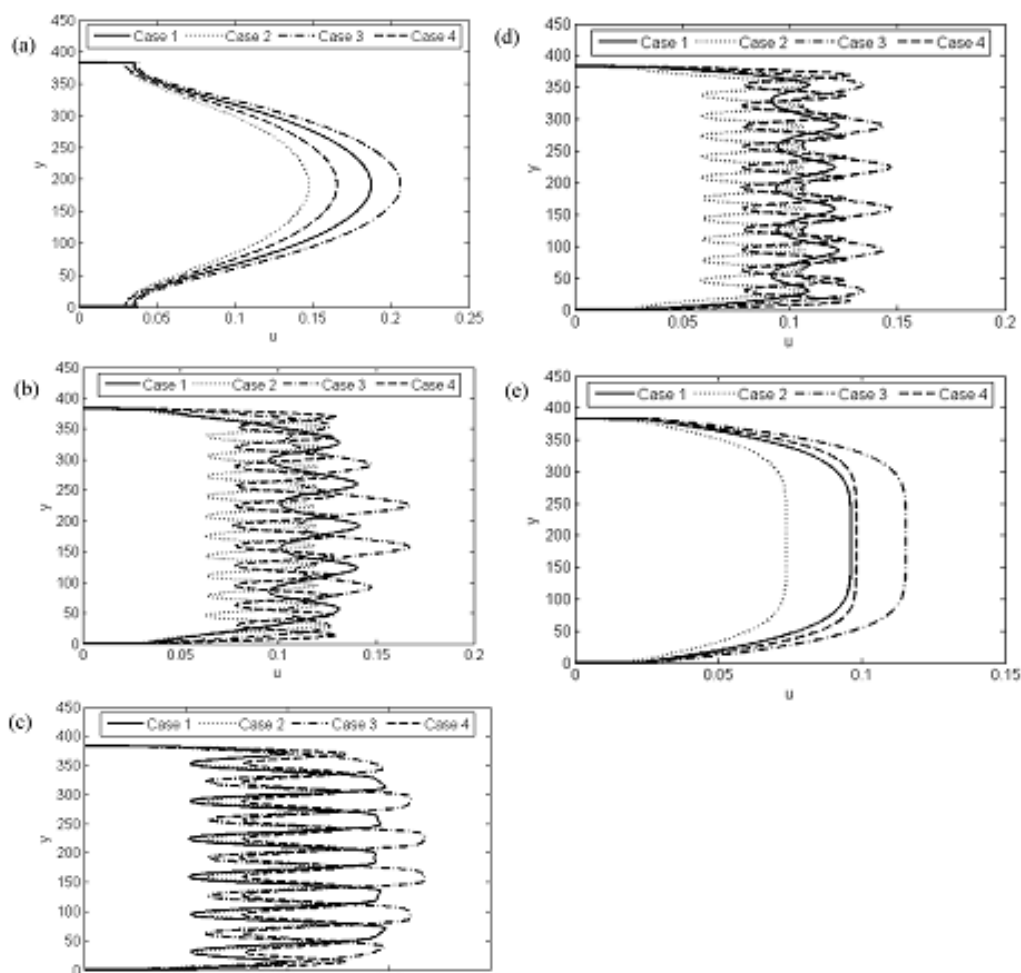


410

411

Fig. 12. Flow streamline around some typical rods in Case 2

412 Fig. 13 shows the flow field at five typical cross sections for Cases 1-4 to investigate the effect
 413 of different arrangements of vegetation on flow structure. Section 1 locates upstream of the
 414 simulated area ($x=118$); Sections 2, 3 and 4 locate at the middle of two adjacent columns of
 415 vegetation ($x=347$, 443 and 539, respectively); and Section 5 locates downstream of the
 416 simulated area ($x=910$).



417

418 Fig. 13. Comparison of the simulated velocities among four typical cases on four typical
 419 cross-sections: (a) Section 1 ($x=118$); (b) Section 2 ($x=347$); (c) Section 3 ($x=443$); (d)
 420 Section 4($x=539$); (e) Section 5 ($x=910$)

421 It is well known that the velocity distribution along transverse direction in a channel without
 422 vegetation is usually parabolic. However, in a channel with vegetation, the velocity distribution
 423 is quite different. Fig. 13 (a) shows that the flow velocity distribution at the upstream of the
 424 vegetation patches is parabolic. It is seen from Fig. 13(a) that the averaged velocities of Cases
 425 1 and 3 are larger than those of Cases 2 and 4 on Section 1, indicating that the flow with sparse

426 vegetation arrangement encounters small flow resistance than that with denser vegetation
427 arrangement.

428 The velocity distributions at Sections 2-4 are indented, as shown in Fig. 13(b), (c) and (d).
429 Right behind each glass rod, flow velocity is smaller due to the blockage effect induced by
430 rods. However, the velocity is larger at other area because of the narrowing of the wetted
431 cross-section area. It can also be found that the averaged velocities of Cases 1 and 3 are larger
432 than those of Cases 2 and 4, respectively.

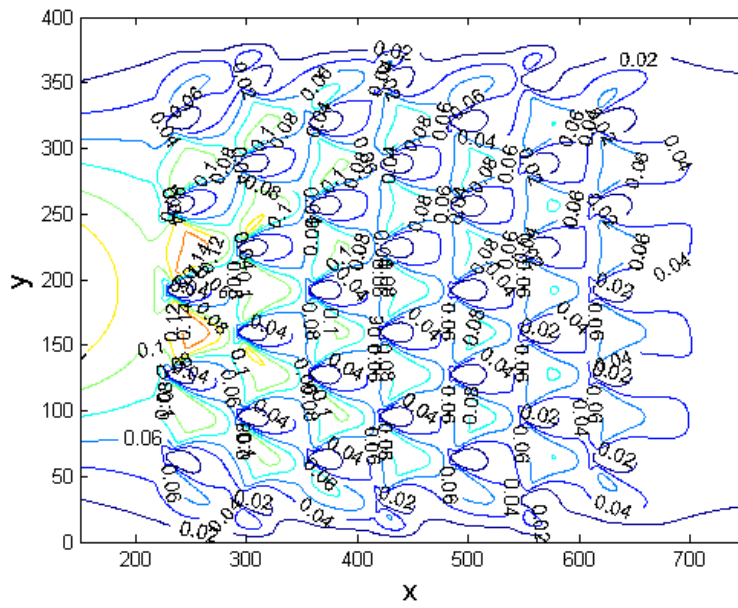
433 The flow on Section 5 is still affected by vegetation-induced drag force. As shown in Fig. 13(e),
434 flow velocity at Section 5 is shown as a U-shape distribution for all these cases, indicating that
435 the flow velocity is close to uniform distribution along transverse direction after the flow
436 passes through the vegetation area. The averaged velocity increase in turn for Case 2, Case 1,
437 Case 4 and Case 3. This means that the flow resistance is the strongest when the rods are denser
438 and staggered, while the flow resistance reaches the weakest when the rods are sparse and
439 parallel. The flow resistance is between the above conditions when the rods are in dense and
440 parallel arrangement, or in sparse and staggered arrangement.

441

442

4.4 Comparison of drag force in the vegetation area

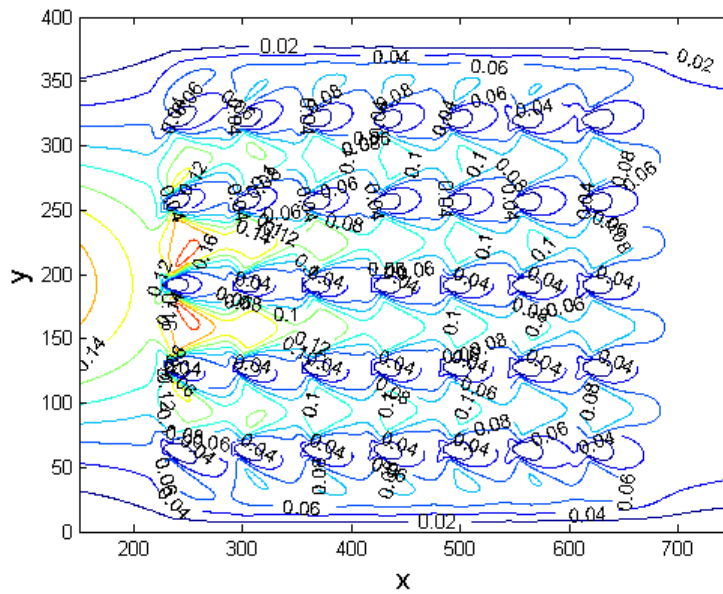
443 Drag force of the vegetation plays an important role in the flow field of vegetation area can be
444 calculated by (20). Because the drag force distributions of four cases are similar, only the
445 contour lines of drag force in Cases 1 and 3 are presented, as shown in Fig. 14. It is seen that
446 the distribution of drag force in the vegetation area is very complicated. Generally speaking,
447 the drag force near the upstream of vegetation area is larger than that downstream.



448

449

(a) Case 1



450

451

(b) Case 3

Fig. 14. The contour lines of drag force in the vegetation area (unit: N/m³)

453

454 5. Conclusion

455 In this study, D2Q9 model in LBM with the numerical algorithm is proposed for numerical
 456 simulation is applied for performing 2D numerical simulation of the flow in an open channel
 457 with unsubmerged rigid vegetation. The MRT-LBE model is applied to improve the stability of

458 LBGK model for flow with high Reynolds number. The vegetation-induced drag force is added
459 in the MRT-LBE model to improve the simulation accuracy.

460 Based on the analysis of the numerical simulated results, the followings conclusions can be
461 obtained:

462 (1) Good agreement between the simulated and measured velocity indicates that the MRT-LBE
463 model is capable of simulating the water flow in open channels with various arrangements of
464 vegetation arrays.

465 (2) The flow velocity distribution is parabolic at cross-sections upstream and U-shaped curve
466 downstream of the vegetation patch in open channel, indicating that vegetation can greatly
467 affect the flow structure downstream to some extent. However, such effect is weaker than that
468 within the vegetation area.

469 (3) The flow velocity is indented distribution at the cross-sections within the vegetation area
470 due to the vegetation-induced drag force. Generally speaking, due to the blockage effect, flow
471 velocity behind a glass rod is relatively small, while the flow velocity between two adjacent
472 rows is relatively large because of the contraction effect.

473 (4) The flow velocity within the vegetation area is larger for sparse arrangements of vegetation
474 than for denser arrangements of vegetation. This is because that the denser vegetation will
475 generate larger flow resistance than the sparse vegetation for otherwise identical conditions.

476 (5) Generally speaking, drag force near the upstream of vegetation area is larger than that
477 generated downstream.

478 (6) The numerical convergence is evaluated for the MRT-LBE model. The order of the
479 numerical convergence is found to be about 1.7.

480

481 **Acknowledgments:** The authors gratefully acknowledge the support of the National Natural
482 Scientific Foundation of China (Nos. 11861003 and 11761005), the Foreign Expert Project of
483 North Minzu University, China. The authors declared that the manuscript does not contain
484 clinical studies or patient data. Reviewers' comments have greatly improved the quality of the
485 paper.

486

487 **References**

488 [1] KANG H. Flow Characteristics and morphological changes in open-channel flows with
489 alternate vegetation zones[J]. **KSCE Journal of Civil Engineering**, 2013,17(5): 1157-1165.

490 [2] DEVI T. B., and Kumar B. Experimentation on submerged flow over flexible vegetation
491 patches with downward seepage [J]. **Ecological Engineering**, 2016,91: 158–168.

492 [3] NEPF H. M. Drag, turbulence, and diffusion in flow through emergent vegetation [J].
493 **Water Resources Research**, 1999,35(2), 479-489.

494 [4] CAROLLO F. G., FERRO V. and TERMINI D. Flow velocity measurements in vegetated
495 Channels [J]. **ASCE Journal of Hydraulic Engineering**, 2002,128: 664-673.

496 [5] CAROLLO F. G., FERRO V. and TERMINI D. Flow resistance law in channels with
497 flexible submerged vegetation [J]. **ASCE Journal of Hydraulic Engineering**, 2005,131(7):
498 554-564.

499 [6] LIU, X., ZHOU, Q., HUANG, S., et al. Estimation of flow direction in meandering
500 compound channels. **Journal of Hydrology**, 2018. 556, 143-153.

501 [7] SHAN, Y.Q., HUANG, S., LIU, C., et al. Prediction of the depth-averaged
502 two-dimensional flow direction along a meander in compound channels. **Journal of**
503 **Hydrology**, 2018, 565, 318-330.

504 [8] WILSON C. A. M. E., STOESSER T. and BATES P. D. et al. Open channel flow through
505 different forms of submerged flexible vegetation[J]. **ASCE Journal of Hydraulic**
506 **Engineering**, 2003,129(11): 847–853.

507 [9] JARVELA J. Effect of submerged flexible vegetation on flow structure and resistance.
508 **Journal of Hydrology**, 2005,307(1-4): 233-241.

509 [10] FOLKARD A. M. Flow regimes in gaps within stands of flexible vegetation: laboratory
510 flume simulations [J]. **Environmental Fluid Mechanics**, 2011,11(3): 289–306.

511 [11] RICARDO A. M., FRANCA M. J. and FERREIRA R. M. L. Turbulent flows within
512 random arrays of rigid and emergent cylinders with varying distribution [J]. **ASCE Journal of**
513 **Hydraulic Engineering**, 2016,142(9): 1-6.

514 [12] LIU C., SHAN Y. Q. and LIU X. N. et al. The effect of floodplain grass on the flow
515 characteristics of meandering compound channels[J]. **Journal of Hydrology**, 2016,542: 1-17.

516 [13] LIU C., NEPF H. Sediment deposition within and around a finite patch of model
517 vegetation over a range of channel velocity. **Water Resources Research**, 2016, 52(1):
518 600-612.

519 [14] NEPF H. M. Flow and transport in regions with aquatic vegetation [J]. **Annual review of**
520 **fluid mechanics**, 2012,44(1): 123-142.

521 [15] NEPF H. M. Hydrodynamics of vegetated channels[J]. **Journal of Hydraulic Research**,
522 2012,50 (3): 262-279.

523 [16] WILSON C. A. M. E., YAGCI O. and RAUCH H. P. et al. 3D numerical modelling of a
524 willow vegetated river/floodplain system[J]. **Journal of Hydrology**, 2006,327(1-2): 13-21.

525 [17] GUO Y. K., ZHANG L. X. and SHEN Y. M. et al. Modelling study of free overfall in a
526 rectangle channel with strip roughness [J]. **ASCE Journal of Hydraulic Engineering**,
527 2008,134(5): 664-668.

528 [18] JING H. F., GUO Y. K. and LI C. G. et al. Three dimensional numerical simulation of
529 compound meandering open channel flow by Reynolds stress equation model [J].
530 **International Journal for Numerical Methods in Fluids**, 2009,59: 927-943.

531 [19] JING H. F. LI C., GUO, Y. K. et al. Numerical simulation of turbulent flows in
532 trapezoidal meandering compound open channels. **International Journal for Numerical**
533 **Methods in Fluids**, 2011, 65:1071-1083.

-
- 534 [20] JING H. F., LI Y. T., LI C. G. Numerical study of flow in the Yellow River with
535 non-monotonous banks[J]. **Journal of Hydrodynamics**, 2016, 28(1):142-152.
- 536 [21] JING H. F., LI C. G. and Guo Y. K. et al. Modelling of sediment transport and bed
537 deformation in rivers with continuous bends[J]. **Journal of Hydrology**, 2013,499: 224-235.
- 538 [22] HUAI, W.X., CHEN, Z. and HAN, J, Mathematical model for the flow with submerged
539 and emerged rigid vegetation. **Journal of Hydrodynamics**, 2009. 21(5): 722–729.
- 540 [23] HUAI W. X., WU Z. L. and QIAN Z. D. et al. Large eddy simulation of open channel
541 flows with non-submerged vegetation [J]. **Journal of Hydrodynamics**, 2011,23(2): 258-264.
- 542 [24] HUAI W. X., XUE W. and QIAN Z. D. Large-eddy simulation of turbulent rectangular
543 open-channel flow with an emergent rigid vegetation patch[J]. **Advances in Water Resources**,
544 2015,80: 30–42.
- 545 [25] MARSOOLI R., WU W. M. Numerical investigation of wave attenuation by vegetation
546 using a 3D RANS model. **Advances in Water Resources**, 2014, 74: 245-257.
- 547 [26] KIM H. S., NABI M., KIMURA I., and SHIMIZU Y. Computational modeling of flow
548 and morphodynamics through rigid-emergent vegetation [J]. **Advances in Water Resources**,
549 2015, 84: 64-86.
- 550 [27] CHEN S. Y., DOOLEN G. D. Lattice Boltzmann method for fluid flows. **Annual Review**
551 **of Fluid Mechanics**, 30:329-364.
- 552 [28] MCNAMARA G. R., ZALESKI G. Use of the Boltzmann equation to simulate lattice gas
553 automata. **Physical Review Letters**, 1998,61(20): 2332-2335.
- 554 [29] AYODELE S. G., VARNIK F. and RAABE D. Lattice Boltzmann study of pattern
555 formation in reaction-diffusion systems[J]. **Physical Review E: Statistical, Nonlinear & Soft**
556 **Matter Physics**, 2011,83(1-2): 4826-4834.
- 557 [30] HUANG R. Z., Wu H.Y. and CHENG P. A new lattice Boltzmann model for solid–liquid
558 phase change[J]. **International Journal of Heat and Mass Transfer**, 2013, 59: 295-301.
- 559 [31] LI Q., LUO K. H. and KANG Q. J. et al. Lattice Boltzmann methods for multiphase flow
560 and phase-change heat transfer[J]. **Progress in Energy and Combustion Science**, 2016,52:
561 62-105.
- 562 [32] JIMENEZ-HORNERO F. J., Giráldez J V, Laguna A M, et al. Modelling the effects of
563 emergent vegetation on an open-channel flow using a lattice model [J]. **International Journal**
564 **for Numerical Methods in Fluids**, 2010, 55(7):655-672.
- 565 [33] YANG Z., BAI F., HUAI W., et al. Modelling open-channel flow with rigid vegetation
566 based on two-dimensional shallow water equations using the lattice Boltzmann method [J].
567 **Ecological Engineering**, 2017, 106:75-81.
- 568 [34] BUXTON G. A. Modeling the effects of vegetation on fluid flow through an acid mine
569 drainage passive remediation system[J]. **Ecological Engineering**, 2018, 110: 27-37.
- 570 [35] GUO Z. L., and SHU C. Lattice Boltzmann method and its applications in engineering.
571 **Word Scientific Publishing Cooperation Limited**, Singapore.2013.
- 572 [36] HE Y. L., WANG Y. and LI Q. Theory and applications of lattice Boltzmann method.
573 **Beijing Science Press**, Beijing, 2009.
- 574 [37] BHATNAGER P. L., GROSS E. P. and KROOK M. A model for collision processes in
575 gases[J]. **Physics Review**, 1954, 94: 511-525.
- 576 [38] MOHAMAD A. A. Lattice Boltzmann method-fundamentals and engineering applications
577 with computer codes[M]. **Springer London Dordrecht Heidelberg**, New York, 2011.

578 [39] QIAN Y. H., D'HUMIERES D. and LALLEMAND P. Lattice BGK models for
579 Navier-Stokes equations [J]. **Europhysics Letters**, 1992, 17, 479-484.

580 [40] D'HUMIERES D. Generalized lattice Boltzmann equations [J]. **In Rarefied Gas**
581 **Dynamics: Theory and Simulations**, 1992, 159: 450-458.

582 [42] LIU C., LIU X. N. and YANG K. J. Predictive model for stage-discharge curve in
583 compound channels with vegetated floodplains [J]. **Applied Mathematics and Mechanics**,
584 2014,35(12): 1495-1508.

585 [42] KAZEMI E. NICHOLS A., TAIT S. J., and SHAO S. D. SPH modelling of depth-limited
586 turbulent open channel flows over rough boundaries[J]. **International Journal for Numerical**
587 **methods in Fluids**, 2017, 83(1): 3-27.

588 [43] GABREIL E., TAIT S. J. SHAO S., and NICOLS A. SPHysics simulation of laboratory
589 shallow free surface turbulent flows over a rough bed [J]. **Journal of Hydraulic Research**,
590 2018, 56(5): 727-747.

591 [44] SHAO S. D., LO E. Y. M. Incompressible SPH method for simulating Newtonian and
592 non-Newtonian flows with a free surface [J], **Advances in Water Resources**, 2003, 26(7):
593 787-800.

594